Thermal Modeling in Metal Additive Manufacturing using Graph Theory: Experimental Validation with In-situ Infrared Thermography Data from Laser Powder Bed Fusion.

M. Reza Yavari¹, Richard J. Williams², Kevin D. Cole¹, Paul A. Hooper², Prahalada Rao^{1*}

¹Mechanical and Materials Engineering, University of Nebraska-Lincoln, Lincoln, NE, USA

²Department of Mechanical Engineering, Imperial College London, UK

Abstract

The objective of this work is to provide experimental validation of the graph theory approach for predicting the thermal history of additively manufactured parts. The graph theory approach for thermal modeling in additive manufacturing was recently published in these transactions. In the present paper the graph theory approach is validated with in-situ infrared thermography data in the context of the laser powder bed fusion (LPBF) additive manufacturing process. We realize the foregoing objective through the following four tasks. First, two kinds of test shapes, namely, a cylinder and cone, are made in two separate builds on a production-type LPBF machine (Renishaw AM250); the material used for these tests is stainless steel (SAE 316L). The intent of both builds is to influence the thermal history of the part by controlling the cooling time between melting of successive layers, called the interlayer cooling time. Second, layer-wise thermal images of the top surface of the part are acquired using an in-situ a priori calibrated infrared camera. Third, the thermal imaging data obtained during the two builds is used to validate the graph theory-predicted surface temperature trends. Fourth, the surface temperature trends predicted using graph theory are compared with results from finite element analysis. The results substantiate the computational advantages of the graph theory approach over finite element analysis. As an example, for the cylinder-shaped test part, the graph theory approach predicts the surface temperature trends to within 10% mean absolute percentage error, and approximately 16 Kelvin root mean squared error relative to the surface temperature trends measured by the thermal camera. Furthermore, the graph theory-based temperature predictions are made in less than 65 minutes, which is substantially faster than the actual build time of 171 minutes. In comparison, for an identical level of resolution and prediction error, the finite element approach requires 175 minutes.

Keywords: Additive Manufacturing, Thermal Modeling, Graph Theory, Validation, Finite Element (FE), Laser Powder Bed Fusion (LPBF), Infrared Thermal Measurements, Interlayer Cooling Time (ILCT).

^{*}corresponding author, email: rao@unl.edu

1 Introduction

1.1 Motivation and Objective

Fast and accurate computational approaches to predict the temperature distribution (thermal history) in additive manufactured parts are valuable for the understanding and prevention of flaw formation, among other critical functions exemplified in Figure 1 [1-4].

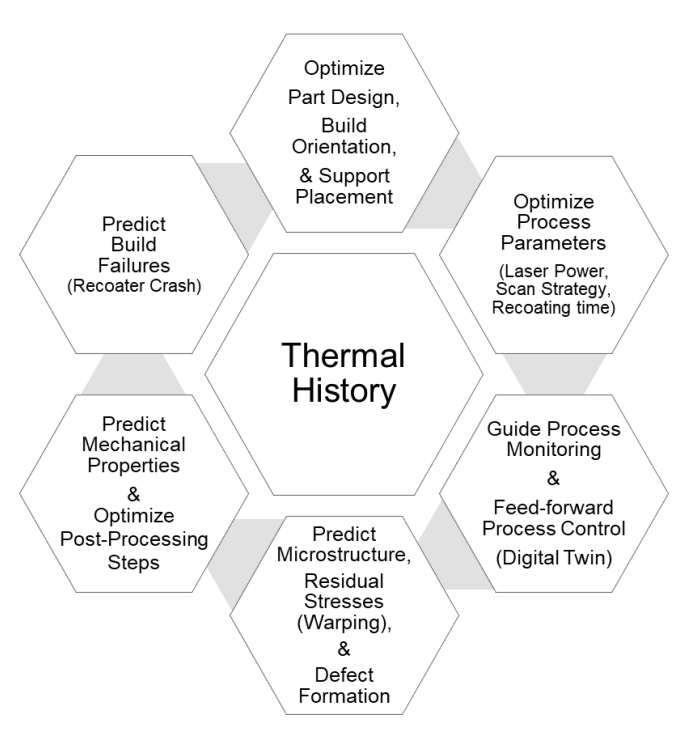


Figure 1: Fast and accurate modeling of the thermal history is central to quality assurance of additive manufactured parts, ranging from physics-based process optimization; monitoring and control; and prediction of part functional properties.

In a previous paper, we proposed a graph theory-based computational heat transfer approach for predicting the thermal history in additive manufactured parts in near real-time [5]. In that paper, the graph theory-predicted temperature trends were verified with: (a) exact analytical Green's function-based solutions, (b) finite element (FE) implementation of Goldak's double ellipsoid moving heat source model [6, 7], and (c) a commercial software for thermal simulation in additive manufacturing (Autodesk Netfabb). Results from our prior work showed that the graph theory approach was about ten times faster than the benchmark Goldak's model implemented in a

commercial FE software (Abaqus) [5]. The mean absolute percentage error of the graph theory-derived predictions relative to FE analysis was less than 10%.

The objective of this paper is to validate the graph theory approach in the specific context of the laser powder bed fusion (LPBF) additive manufacturing (AM) process using in-situ infrared thermal measurements. In LPBF, metal powder is deposited on a bed (build plate) and selectively melted layer-upon-layer with a laser. The temperature gradients induced in the part during LPBF is one of the main causes for flaws such as cracking and distortion in shape [2, 4].

1.2 Approach and Novelty

To realize the foregoing objective, we frame the following four tasks:

- (1) Two test part geometries are made in two separate builds on a Renishaw AM250 productiongrade LPBF system. The two test parts are described below.
 - (i) A cylinder of diameter 8 mm and height 60 mm. The test cylinder is sintered alongside eight other identical cylindrical-shaped parts on the build plate. The total time for the build is 171 minutes (1200 layers).

The build plan for the test cylinder has three phases. First, for the first 20 mm vertical height of the test cylinder, it is scanned simultaneously with the rest of the eight cylinders. In the second phase, the test cylinder is processed to a total height of 40 mm, while the scanning of the rest of the eight other cylinders is paused. The third and concluding phase is identical to the first phase – the test cylinder is processed to its final height of 60 mm along with the rest of the eight cylinders.

The preceding build strategy, where some parts are intermittently scanned, leads to a variation in the time required by the laser to process a layer, because, the laser takes longer to complete a layer in the first and third phases when more parts are scanned, compared to the second phase.

Accordingly, the time elapsed between the processing of two successive layers – called the interlayer cooling time (ILCT) – varies across the build. The layer-to-layer variation in ILCT leads to microstructural heterogeneity in LPBF parts [8].

(ii) Inverted cone shape with a bottom diameter of 2 mm, top diameter of 20 mm, and vertical build height of 11 mm. The build time is nearly 51 minutes (220 layers). The gradual increase in the surface area of the cone as a function of its vertical build height causes a variation in the ILCT.

Simple cylinder and cone-shaped test parts is used because the ILCT can be readily determined compared to complex-shaped parts; the ILCT is a critical input parameter for model validation.

- (2) Surface temperature measurements for the two test parts are acquired layer-by-layer using an in-situ longwave infrared thermal camera. The surface temperature measurements is recorded over their entire build duration consisting of 1200 and 220 layers for the cylinder and inverted cone shapes, respectively. To the best of the authors' knowledge, model validation efforts documented in the literature use in-situ temperature measurements from at most 25 layers.
- (3) The steady state surface temperature for the two test parts is predicted using the graph theory-based approach and subsequently validated layer-by-layer relative to the experimental measurements acquired using the thermal camera.
- (4) The layer-by-layer thermal history predictions from the graph theory predictions are compared with a previously published FE model [9]. The comparison of FE and graph theory approach includes predictions of the steady state surface temperature, as well as the temperature at a point in the interior of each of the two test parts.

1.3 Organization of the paper

The rest of this paper is structured as follows. In Section 2, we review the prior literature and delineate the challenges involved in the acquisition of thermal history in LPBF. Section 3 describes the experimental methodology, and adaption of the graph theory and FE approaches to predict the surface temperature. Section 4 reports results concerning the validation of the graph theory with experimental measurements, and comparison with FE analysis. Lastly, conclusions and avenues for future work are summarized in Section 5.

2 Review of Prior Work and Challenges in Temperature Measurement in Metal AM

Articles by Yan *et al.* [10], and Tapia and Elwany [11] review in-situ thermal measurement approaches in AM. There are two approaches to obtain part-level in-situ temperature in LPBF. The first approach is to embed thermocouple(s) inside the part or in the substrate. The second approach uses thermal imaging to measure part surface temperature [12, 13]. This work applies the second strategy. In the next two sub-sections, Sec. 2.1 and Sec. 2.2, we highlight the key challenges in both the thermocouple and infrared thermography approaches, respectively, and justify the use of infrared thermography as a viable means to validate the graph theory-based thermal model.

2.1 Measurement of the Temperature Distribution in LPBF using Contact-Based Thermocouples.

The temperature profile at discrete points in LPBF parts is obtained by embedding thermocouple(s) (i): inside the substrate, (ii) incorporating thermocouples inside a pre-built part(s) and then building the test part(s) over the pre-built part(s). To the best of the our knowledge, there are no examples in the literature that describe stopping the LPBF process to instrument thermocouples inside the test part.

Researchers have acquired the temperature trends at the underside of the part by brazing thermocouples on the surface of the build plate in a manner such that the head of the thermocouple is barely exposed [12, 13]. However, it is observed that the temperature signals obtained by the thermocouple inside the substrate is considerably attenuated as the part grows in size.

For example, Dunbar *et al.* embedded both a thermocouple and strain gage array within the build plate of an EOS M270 machine to validate their predicted distortion trends [12, 13]. In their setup, the sensor array is coupled to a battery-powered data acquisition system incorporated underneath the build plate. Thermocouples are drilled through the build plate, such that the tip of a thermocouple is exposed (≈ 0.25 mm) above the build plate, and care is taken to insulate the underside of the thermocouple(s). The build dimensions for the test coupons used by Dunbar *et al.* are 6.25 mm \times 6.25 mm \times 2.33 mm (vertical build height), and the experiment lasts 10 minutes, in which temperature data is acquired for a maximum of three layers.

Promoppatum *et al.* [14] used a setup similar to that of Dunbar to acquire temperature data for a large 165 mm × 60 mm × 70 mm (vertical build height) stainless steel part. Temperature trends at five discrete points on the underside of the part is tracked using thermocouples. The temperature readings recorded by the thermocouples at the underside of the part reduced to a steady state temperature of 200 °C within 25 layers.

Similar attenuation of the temperature signature acquired by a thermocouple embedded in the substrate is also observed in a recent work of Hoelzle *et al.* [15]. Experiments were conducted on a custom experimental open architecture LPBF setup at Edison Welding Institute. Prebuilt cuboid-shaped stainless steel coupons of ~12 mm × 12 mm × 12 mm size were embedded with four thermocouples at different layer heights, and one thermocouple was embedded into the build plate. In one of their tests, Hoelzle *et al.* [15] deposit a total of five layers (200 µm total thickness) on

the prebuilt coupons. Thermocouple data was acquired for roughly 7 seconds per layer. The thermocouple embedded in the build plate did not register any temperature variation.

Researchers have obtained the temperature trends at discrete points inside the part and substrate in the directed energy deposition (DED) AM process. In DED, because the part is not surrounded by powder, a thermocouple can be readily embedded onto the substrate or spot welded on the surface of the part by stopping the process as demonstrated in the work of Heigel *et al* [16]. In one of our prior works, we validated the graph theory approach for the DED process with temperature data obtained from thermocouples embedded inside the substrate for titanium alloy test parts [17].

The preceding literature review highlights the difficulty in obtaining the thermal history at discrete points via contact-based thermocouples embedded inside the LPBF substrate or part as the temperature signature attenuates after a few layers.

2.2 Measurement of the Temperature Distribution in LPBF using Infrared Thermography.

Given the challenge in measurement of temperature trends in the inside of the part with thermocouples in LPBF, researchers frequently use a thermal camera to obtain the relative temperature trends on the top surface of the part before the next layer of powder material is deposited [11, 18-21]. The infrared camera is typically mounted either inside or outside the chamber at an angle to the powder bed – called staring configuration. However, the surface temperature data acquired by the thermal camera is a relative measurement and not the absolute surface temperature [18, 19, 22-24]. Hence, the temperature readings captured by the thermal camera must be calibrated *a priori* under practical LPBF conditions so that they can be scaled to absolute temperature measurements.

Researchers at the National Institutes of Standards and Technology (NIST) report different approaches to calibrate thermographic measurements in LPBF [18, 19, 22]. One such approach uses the concept of a black body emitter to calibrate the thermal camera measurements [18]. This approach is exemplified by Rodriguez *et al.* [25]. The key idea is to embed a thermocouple inside a deep cavity drilled in an AM test part. When the part is heated, the cavity inside the object behaves as a black body emitter per Planck's law. As the part is heated in a controlled manner to a steady state temperature, the absolute temperature readings measured by the thermocouple are used to scale (calibrate) the surface temperature readings measured by a thermal camera. In this work, we use the black body emitter approach to calibrate the thermal camera. The calibration procedure is summarized in Sec. 3.2 and described in detail in Ref. [8].

3 Methods

3.1 Experimental Setup

The schematic of the experimental setup is shown in Figure 2; further details are reported in Ref. [8]. A longwave infrared (LWIR) thermal camera (FLIR A35X) with a spectral range of 7.5 µm to 13 µm is incorporated within the build chamber of a Renishaw AM250 LPBF machine. The thermal camera is sealed inside a vacuum-tight box with a germanium window and focused onto the build plate inclined at an angle of 66° from the horizontal. The configuration of the infrared thermal camera allows the measurement of surface temperature of the entire top surface of the part.

Thermal images are captured at a resolution of 320×256 pixels, providing a pixel resolution of approximately 1 mm², and recorded at a rate of 60 frames per second. The response time for the sensor is approximately 12 milliseconds. the calibration process used in our previous works is briefly described in the forthcoming section (Sec. 3.2) [8].

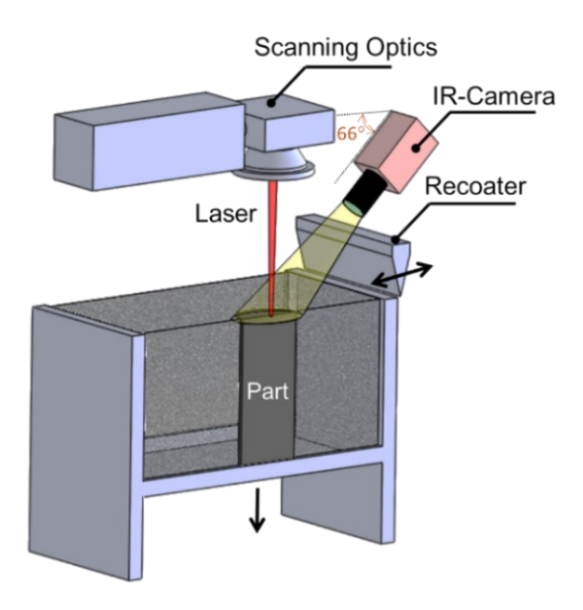


Figure 2: The schematic of the experimental setup used in this work; surface temperature data is acquired by a longwave infrared camera inclined at an angle of 66° to the horizontal plane.

3.2 Calibration of the Thermal Camera Measurements to Absolute Temperature

To calibrate the temperature trends captured by the thermal camera, a cylinder-shaped test artifact is made using LPBF. The calibration test artifact is identical in geometry, material (SAE 316L), and LPBF processing parameters used for the two experimental builds (Sec. 3.3). The calibration setup is shown in Figure 3 is adapted from Ref. [8].

The temperature of the calibration artifact is controlled using a 200 W cartridge heater embedded in a recess in the bottom. The calibration artifact is heated, and its resulting surface temperature is recorded using two thermocouples located in two respective recesses milled on its top surface. One of these thermocouples (TC1 in Figure 3) is used as a feedback control for the cartridge heater, while the other (TC2) records the temperature trends used for calibration.

The thermal camera is calibrated in the range of 300 K to 800 K because the maximum temperature to which the cartridge heater is operational is 800 K. A 9-pixel × 9-pixel (9 mm²) sample of thermal intensity values in the center of the top surface of the calibration artifact are extracted from the thermal camera data.

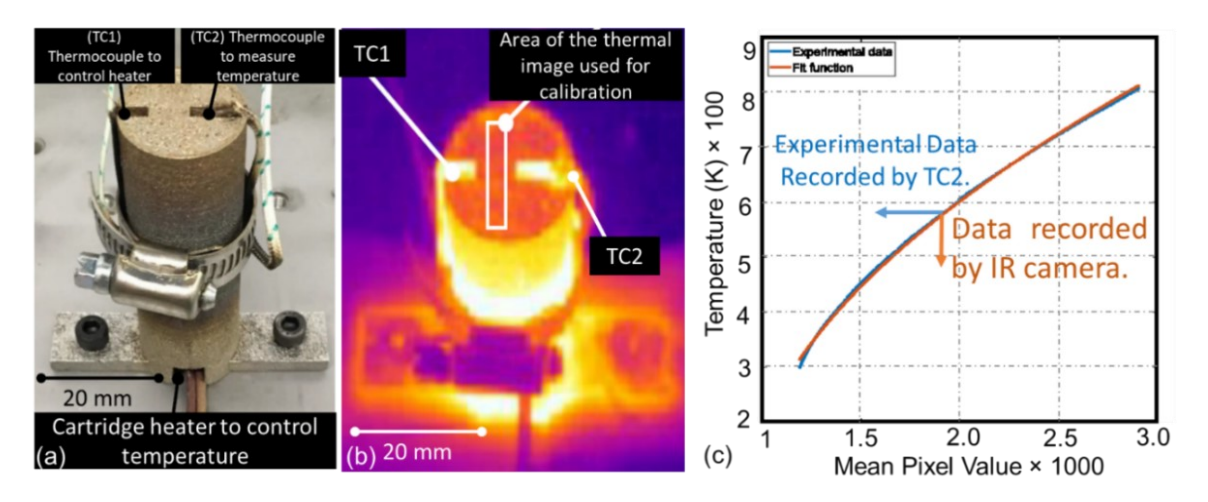


Figure 3: The calibration procedure used for the thermal camera (adapted from Ref. [8]). (a) two thermocouples are located inside a slot in an LPBF part which is identical to the cylindrical part from Build 1. (b) the heating of the part with a cartridge heater to simulate the rise in temperature. (c) the calibration function of actual temperature measured by the thermocouple vs. the data recorded by the IR camera.

A calibration function (Figure 3(c)) is obtained by fitting the average intensity over the 9-pixel × 9-pixel sample area recorded by the thermal to the mean temperature recorded by the thermocouple TC2. To ascertain the uncertainty in the thermal camera readings the calibration procedure is repeated ten times (n = 10). The 95% confidence interval in temperature readings in the interval of 300 K to 800 K ranged from 0.1% to 1% of the mean temperature reading [8]. For temperature readings beyond 800 K, we expect the calibration function to remain valid, as it is derived from Planck's law and the emissivity would not change significantly until melting occurs (viz., 1643 K).

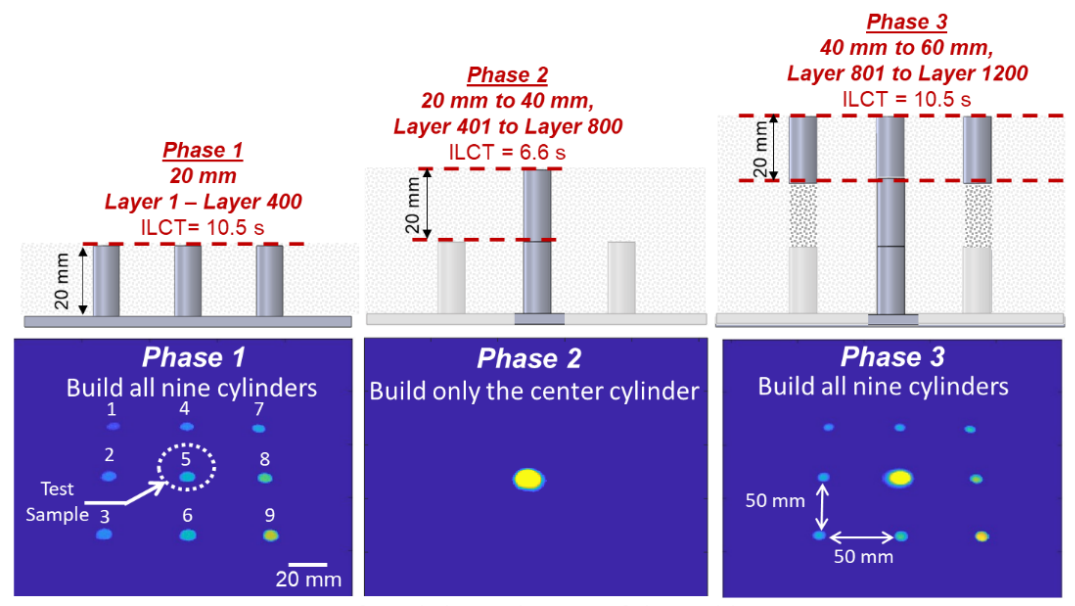
The calibration procedure is repeated with a thin layer of unmelted powder deposited on top of the calibration artifact, and the test data is used to derive another calibration curve. Such a two-part calibration procedure, with a solid part, and with unmelted powder layered on top, ensures that the temperature readings account for the change in material emissivity in LPBF after a layer is fused (but before a new layer is recoated), and after a new layer is added (but before it is melted).

3.3 Experimental Builds

In this work, we make two LPBF test parts in two different builds that are designed to influence the surface temperature in the part through variation in the ILCT. The scan pattern, process parameters and material properties for the two builds are reported in Table 1.

3.3.1 Build 1 – Inducing variation in the interlayer cooling time by altering the build plan.

The test part is a cylinder of diameter 8 mm and height 60 mm in the center of the build plate. This cylindrical test part is built in three phases, as depicted in Figure 4. The test part is built with a laser power of 200 W, while the rest of the eight other cylinders are built at 5 W; all parts are built without anchoring supports. As we will explain shortly, building the rest of the eight cylinders prevents their collapse during Phase 3 of Build 1.



Infrared Thermal Image of the Build

Figure 4: The three phases in building the cylinder-shaped part. The total build time is 171 minutes and consists of 1200 layers; each phase has 400 layers. The test part (sample) is the central cylinder. Shown in the top is the front view, with the change in the interlayer cooling time (ILCT) depending on the number of parts being processed in a layer. Shown in the bottom is the corresponding infrared image of the test part (central cylinder) captured by the thermal camera. All the cylinders are built without supports. The center cylinder is built at a laser power of 200 W, the rest of the eight cylinders are built at 5 W.

In Phase 1, the test part is built along with eight other identical cylinders arranged in a grid pattern. The ILCT in Phase 1 is roughly 10.5 seconds. After a build height of 20 mm is reached (400 layers, each layer is 50 µm), the processing of the rest of the cylinders is stopped, marking the end of Phase 1, and start of Phase 2. In Phase 2, only the test sample, i.e., the center cylinder is processed until a total build height of 40 mm is reached (800 layers). Because only one cylinder is processed, the ILCT reduces to nearly 6.6 seconds from 10.5 seconds in Phase 1. Lastly, in Phase 3, all nine cylinders are again processed for a total build height of 60 mm (1200 layers). Accordingly, in Phase 3, the ILCT again increases from 6.6 seconds to approximately 10.5 seconds. The total build time is about 171 minutes.

In Phase 3, because there is un-melted powder underneath the rest of the eight cylinders – there are no anchoring supports below the part, the parts will tend to move and cause a build failure. Hence, the laser power for melting of the eight cylinders around the periphery of the test sample is always set at a minimum of 5 W. In other words, the scanning of the rest of the eight cylinders at low power allows them to be built without supports.

Table 1: Summary of the material and processing parameters used in this work for Build 1 and 2.

Process Parameter	Values [units]
Laser type and wavelength.	200 W fibre laser, wavelength 1070 nm
Laser power, point distance, exposure time	200 W, 60 um, 80 us
Inner border parameters - power, point distance, exposure time for the test part (center cylinder)	200 W, 40 um, 90 us
Outer border parameters - power, point distance, exposure time (center cylinder)	110 W, 20 um, 100 us
Hatch spacing	110 um
Layer thickness	50 um
Spot diameter of the laser	65 um
Scanning strategy for the bulk section of the	Meander-type scanning strategy without
part	rotation of scan path between layers.
Build atmosphere	Argon
Material Properties	Values [units]
Material type	316L stainless steel
Particle size	10-45 um

3.3.2 Build 2 – Inducing variation in the interlayer cooling time through the part geometry.

The test part devised for this build is shown in Figure 5; it is an inverted cone whose diameter gradually increases from 2 mm to a diameter 20 mm over a vertical build height of 11 mm (50 μ m layer thickness, 220 layers). The build time is about 51 minutes.

In this test part, the ILCT increases almost linearly in proportion to the build height from 10 seconds at the start of the build to 16 seconds at the final 11 mm build height. Furthermore, the temperature of the top surface increases progressively with the deposition of new layers as the narrower cross-section of the part in the preceding layers impedes the diffusion of heat.

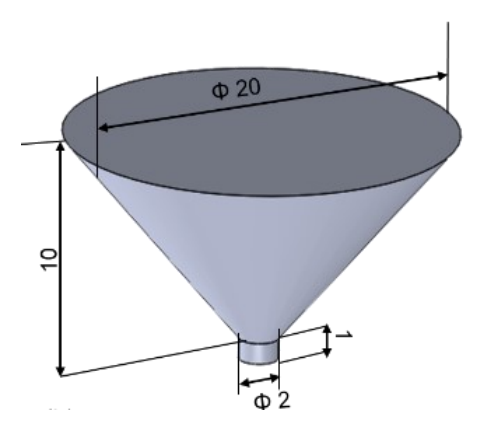


Figure 5: The schematic of the inverted cone geometry implemented in Build 2. The total build time is 51 minutes, and consists of 200 layers of 50 μ m.

3.4 Procedure for obtaining the steady state surface temperature from the thermal camera images.

We process the surface temperature data (T(t)) acquired by the thermal camera to obtain the steady state surface temperature between two immediate layers. The steady state temperature between layers k and k+1 is represented as \overline{T}_k^{k+1} . The steady state temperature \overline{T}_k^{k+1} is derived from the time-varying surface temperature T(t) acquired from the thermal camera using the following steps.

As explained in Sec. 3.2, the surface temperature T(t) is the temperature averaged over the 9 mm² area encompassing the center of the part, which corresponds to a 9-pixel × 9-pixel region of the thermal camera image (Figure 3). Referring to Figure 6, the surface temperature signal T(t) is distilled into three steps common to both Build 1 and Build 2. The y-axis of Figure 6 is T(t) in Kelvin. The x-axis is time in seconds; each data point is processed from a frame of the thermal camera (frame rate 60 Hz).

Step 1: Large upward spike denoting the beginning and end of melting

In this stage of the process, the laser is active (ON), and is currently scanning the powder bed. A large upward peak is observed when the laser is directly sintering the 9 mm² area sampled from the thermal image. The large upward spike lasts less than 0.5 seconds (30 thermal image frames). The time from the end of the large upward spike to the start of the next upward spike is the ILCT.

Precise quantification of the ILCT is critical for model validation purposes; the time t = ILCT in Eqn.(1), Sec. 3.5. However, the ILCT is not constant, but can change between layers depending on the build plan and shape of the part. As we will show in Sec. 4.1, for Build 1 the ILCT for Phase 1 and Phase 3 is approximately 10.5 sec, which is considerably longer than the ILCT for Phase 2 which is 6.6 sec. In Build 2 the ILCT increases continually over the build from 10 sec to 16 sec. In this work the ILCT is tracked using an spike detection procedure in Matlab.

Step 2: First downward spike due to the recoater blocking the field-of-view of the IR camera when it returns to the powder reservoir.

After the end of melting of a layer, the recoater returns to fetch fresh powder. During Step 2, the bed is lowered so that the recoater can pass freely over the powder bed and avoid contact with the part. As the recoater returns to fetch fresh powder, the IR camera field-of-view is momentarily blocked leading to a large downward spike in temperature lasting less than a 1/50th of a second.

Step 3: Second downward spike due to new powder being deposited on the powder bed when the recoater rakes a new layer of powder on the surface of build plate.

As the recoater makes another pass to deposit a fresh layer of powder, it again momentarily blocks the field-of-view of the IR camera causing a large downward spike in the signal. Because the recoater speed is considerably slower than in the previous Step 2, hence the downward peak lasts for close to 1/5th of a second.

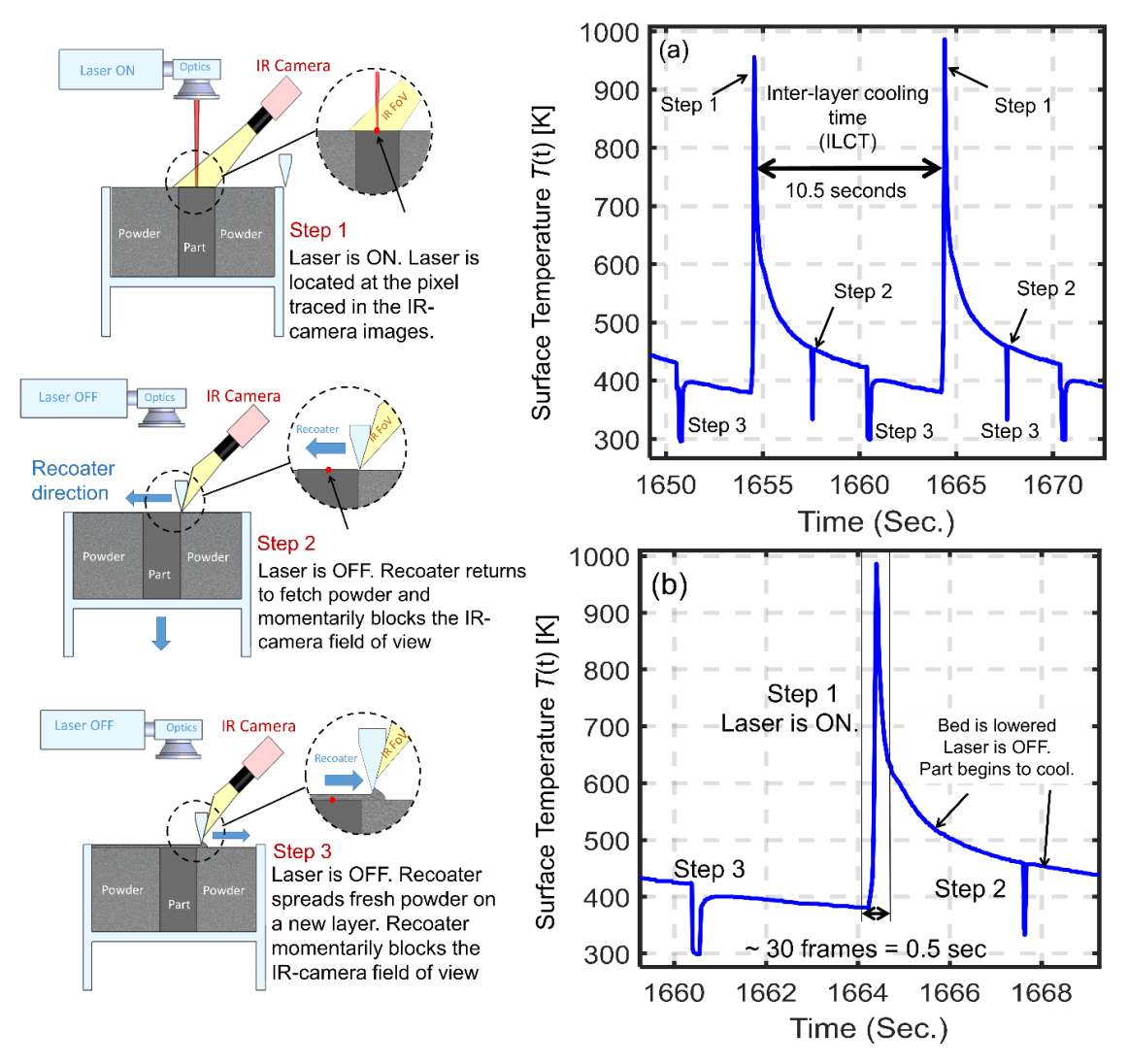


Figure 6: The physical process-related reasons for the spikes observed in the thermal camera images. (a) The three large periodic spikes in the temperature and the schematic representation of why these spikes occur. (b) zoomed in portion of the thermal camera signature. This signal is for Phase 1 of Build 1, according the ILCT is 10 seconds.

When the powder is initially spread it is at ambient temperature (300 K). Therefore, the powder will extract heat from the solidified part surface which is still at a higher temperature. The heat required to raise the powder temperature will cause the surface temperature of the part to decrease. This drop in the surface temperature of the part due to the deposition of fresh powder is accounted in the separate powder-related step in the calibration of the infrared camera as described in Sec. 3.2. The corrected temperature signature is overlaid on the surface temperature signal in Figure 7(a). The steady surface temperature readings for layer k and k+1, \overline{T}_k^{k+1} , is the temperature in the relatively flat portion of the curve in Figure 7(b) before layer k+1 is processed. Described another way \overline{T}_k^{k+1} is the minimum temperature recorded just before melting of the new layer.

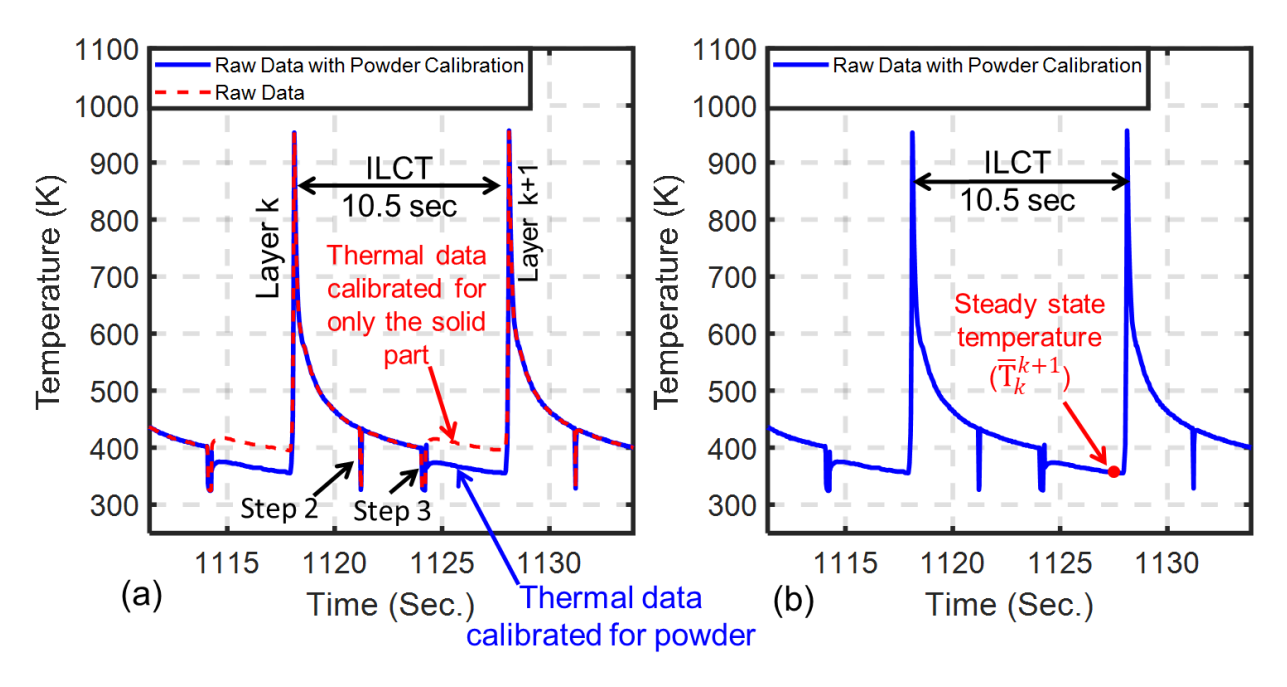


Figure 7: (a) The surface temperature signature (dotted line) obtained before applying the calibration to account for deposition in powder. Note the slight increase in temperature after Step 3. The solid line shows the temperature after calibration of the thermal camera to account for deposition of the powder (note the \approx 40 K difference between the powder calibrated, and uncalibrated measurements). (b) The steady state temperature is obtained just prior to the sintering of the fresh layer.

3.5 Procedure for Application of the Graph Theory Approach

The graph theory approach is illustrated schematically in Figure 8 in the context of Build 1. These steps are discussed in detail in our previous works [5, 26]. The graph theory approach, as explained in our previous work, converts the part geometry into a set number of discrete nodes [5].

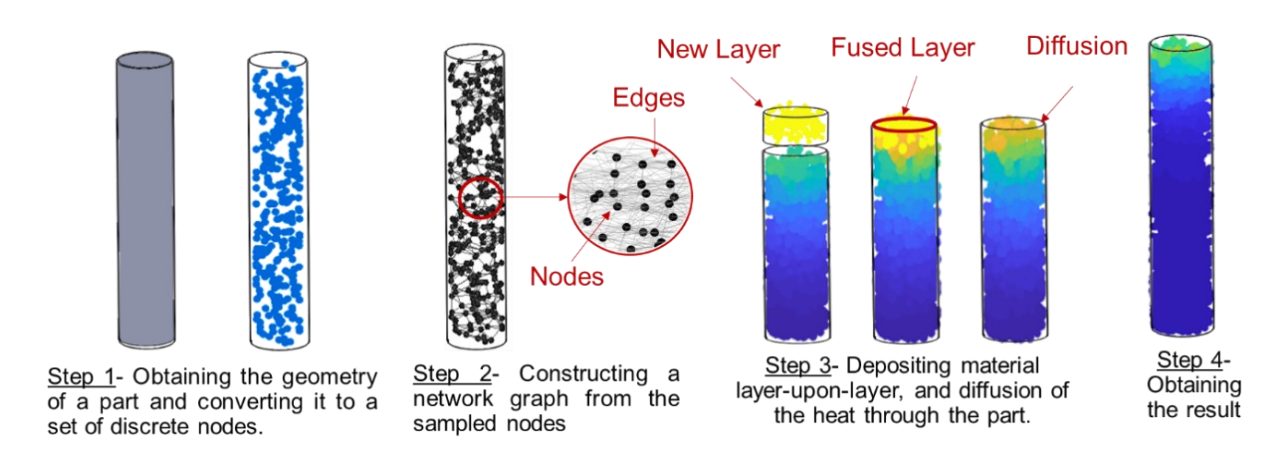


Figure 8: The four steps in the graph theory approach as applied to the cylindrical part described in Build 1. The mathematical details are described in [5].

A network graph is constructed over these nodes, and heat diffusion over the graph is studied layer-by-layer. If the temperature at each node is arranged in matrix form, the instantaneous temperature **T** after time t (=ILCT) is obtained as a function of the Laplacian eigenvectors ($\boldsymbol{\phi}$) and eigenvalues ($\boldsymbol{\Lambda}$), with T₀ (= 1600 K) as the melting point of the material (SAE 316L),

$$\mathbf{T} = \mathbf{\Phi} e^{-\alpha \mathbf{g} \mathbf{\Lambda} t} \mathbf{\Phi}' \mathbf{T}_0 \tag{1}$$

We reiterate that in this work, only the surface temperature is available for validating the predictions from the graph theory approach. Further, the temperature predictions for every node in the interior of the part at each time step is readily obtained at no additional computation cost. To demonstrate this possibility, we track the temperature trends for a point in the interior of the test parts, and verify these trends with FE analysis in Sec. 4.3.

To maintain consistency with the calibrated thermal data, the temperature distribution predictions for the graph theory model are validated against the same 9 pixel × 9 pixel sample region on the surface of the test part shown in Figure 3. While validation of the graph theory predictions with temperature measurements nearer to the edges of the test part would be valuable, we are constrained by the limited 1 mm² resolution of the thermal camera used in this work. The part-powder boundary involves complex phenomena encompassing convective and conductive heat transfer modes, compared to the dominance of conduction-based heat loss near to the center of the part, therefore, the measurement uncertainty at the edges of the part would become overwhelmingly large.

3.5.1 Simulating deposition of multiple layers at once (super layer or meta-layer approach) to reduce the computation time.

To mitigate the computation time, instead of simulating the deposition one individual layer (layer height 50 µm) at a time, we adapt the graph theory approach to simulate the deposition of several layers at a time. Such a layer consolidated from two or more individual layers is called a *super layer or meta layer*, and is commonly used in coarse FE modeling of the AM process to reduce the computation time [9].

Using the super layer approach is particularly well suited to the graph theory method as the precision is independent of the simulated time step. This is because the time t for which the heat is diffused in the part in Eqn. (1) can be set to one large time step without computing the temperature at intermediate discrete steps as in FE analysis. In this work, the time t is set to the interlayer cooling time (ILCT) accrued over super layers. In this work, the super layer is varied from 3 mm (consisting of 60 individual layers of 50 μ m each) to 0.3 mm (6 individual layers).

3.5.2 Tuning the graph theory model parameters

The graph theory simulation studies require tuning of two types of factors.

(1) Number of Nodes (N)

Selecting the total number of nodes (N) into which the part is discretized involves a tradeoff in computation time and accuracy [5]. In our previous work for a complex geometry part, selecting a higher number of nodes results in a smaller error in comparison to benchmark FE studies, while degrading the computational efficiency [5]. In this work, we evaluated the effect of varying the number of nodes from 1000 to 5000 in steps of 1000.

(2) Model Parameters related to heat diffusion.

In the graph theory approach two model parameters related to the heat diffusion must be determined, namely, the gain factor (g) Eqn. (1), and the neighborhood distance (ε) which governs the connectivity of the nodes [5]. There is an interaction between these two parameters. To mitigate this complexity, and need for extensive tuning, in this work we have made one change to the graph theory model, instead of setting ε to an absolute distance in mm, we now connect the nearest 50 neighbors of a node with edges. The number 50 is selected based on extensive offline studies.

We report the mean absolute percentage error (MAPE) and root mean square error (RMSE, Kelvin) for each tested combination of super layer thickness and number of nodes. To obtain the gain factor (g), we fix the total number of nodes at 1000, and conduct a grid search with respect to the infrared thermal measurements obtained for Phase 1 of Build 1. To make the calibration more rigorous, the layer height set in the simulation for the calibration of g studies is 50 μ m, which is the same as the layer height of the build – i.e., the super layer is set equal to actual layer height for model calibration.

The value of g is changed with the number of nodes (N) fixed at 1000 and layer thickness 50 μ m. The graph theory approach is applied for the first 20 mm of the build height, i.e., the graph theoretic model is calibrated for the temperature readings from Phase 1 of Build 1. The results from the model calibration procedure are shown in Figure 9(a). The value of g that minimizes the MAPE and RMSE is selected. The results from the grid search are shown in Figure 9(b). The value of g that minimizes MAPE and RMSE is 1.5×10^4 ; this value is set constant for all subsequent simulation studies, including Phase 2 and Phase 3 of Build 1, and entirety of Build 2.

The rest of the material-related constants and simulation parameters are described in Table 2. The simulations are conducted in the MATLAB environment on a desktop personal computer with an Intel Core i7-6700 CPU, clocked at 3.40 GHz with 32 gigabytes of onboard memory.

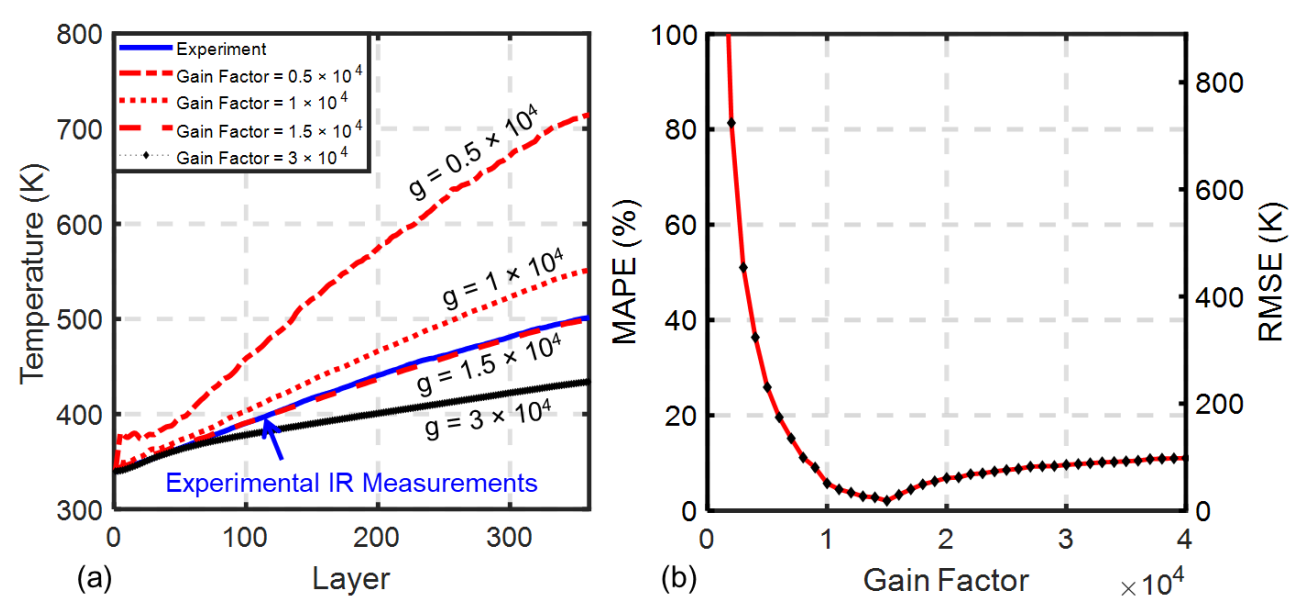


Figure 9: (a) Representative steady state surface temperature trends obtained for Phase 1 of Build 1 by varying the gain factor (g). (b) The mean absolute percentage error (MAPE) and root mean squared error (RMSE, in Kelvin).

Table 2: Summary of the simulation parameters used in this work.

Simulation Parameters	Values			
Super layer thickness [mm]	Varies from 3 to 0.3 mm for Build 1 (Cylinder) and from 1 to			
Super layer unexhess [mm]	0.2 mm for Build 2 (Inverted Cone)			
Total number of nodes in the part (N)	Varies from 1000 to 5000 in steps of 1000			
Node Density (N per mm ³)	Varies from 0.3 to 1.6 for Build 1 (Cylinder) and from 0.8 to			
rode Bensity (iv per inini)	4.3 for Build 2 (Inverted Cone)			
Number of neighbors which is	50			
connected to each node.				
Gain factor (g)	1.3×10^4			
Convection coefficient wall to powder,	1×10^{-5}			
$h_w [W \cdot m^{-2} \cdot K]$				
Convection coefficient substrate (sink),	1×10^{-2}			
$h_s [W \cdot m^{-2} \cdot K]$				
Thermal diffusivity (α), [m^2/s]	3×10^{-6}			
Density, ρ [kg/m ³]	8,440			
Melting Point (T_0) (K)	1,600			
Ambient temperature, T_{∞} (K)	300			
Processing hardware	Intel Core i7-6700 CPU, @3.40 GHz with 32 GB RAM.			

3.6 Procedure for Verification with Finite Element (FE) Analysis

The FE approach used for predicting the thermal history in LPBF parts is detailed in our previous publication [9]. To maintain parity, the FE model uses the identical meta-layer or super layers implemented for the graph theory approach. In our prior work, we obtained both the temperature distribution and distortion in an LPBF part by simulating the deposition of super layers. The FE predicted thermal-induced distortions are within 10% of offline measurements [9].

To ensure equitable comparison of FE and graph theory approaches the following steps are taken: (i) for both the FE and graph theory implementations MAPE and RMSE are quantified in for the same number of nodes and resolution (super layer thickness); (ii) we compare the computation time required by the FE predictions to converge to approximately the same MAPE and RMSE of the graph theory predictions at an identical level of resolution. Lastly, we qualitatively compare the FE and graph theory predictions for a point in the interior of the two test parts; there is no additional computation cost associated with calculating the temperature distribution at an interior point.

4 Results

4.1 Results for Build 1

4.1.1 Thermal signatures acquired from the thermal camera.

The surface thermal signatures recorded for Build 1 are shown in Figure 10. The y-axis in Figure 10(a) is the surface temperature T(t). In Figure 10(b) the steady state surface temperature between two successive layers (\overline{T}_k^{k+1}) is tracked on the y-axis. Changes in the temperature trend across the three phases of Build 1 are more clearly evident in Figure 10(b) on processing the temperature signatures T(t) from Figure 10(a).

A gradual increase in the steady state surface temperature is observed during Phase 1, succeeded by a sharp increase observed at the start of Phase 2, and finally followed by a drop at the start of Phase 3. These changes in the temperature correspond to the change ILCT; the reason for the sharp increase in temperature in Phase 2 is the decrease in ILCT to roughly 6.6 seconds (Figure 10(d)), compared to 10.5 seconds in Phase 1 and Phase 3 (Figure 10(c)).

To summarize these observations, in Build 1, the ILCT, and consequently, the surface temperature distribution of the cylindrical test part changes considerably from Phase 1 through 3. These temperature trends from Build 1 have two practical implications, as shown in our previous work [8]. First, tasks that require stopping the build, e.g., replenishing the power, re-filling the chamber with inert gas, that entail a change in the ILCT are liable to cause microstructural heterogeneity. Second, it is not viable to optimize the process parameters for one type of geometry, and consider this knowledge as transferable to other situations – the process parameters must be demarcated through *in-silico* thermal experiments for every build if there is any change in the part geometry, orientation, build layout, number of parts, and scanning strategy.

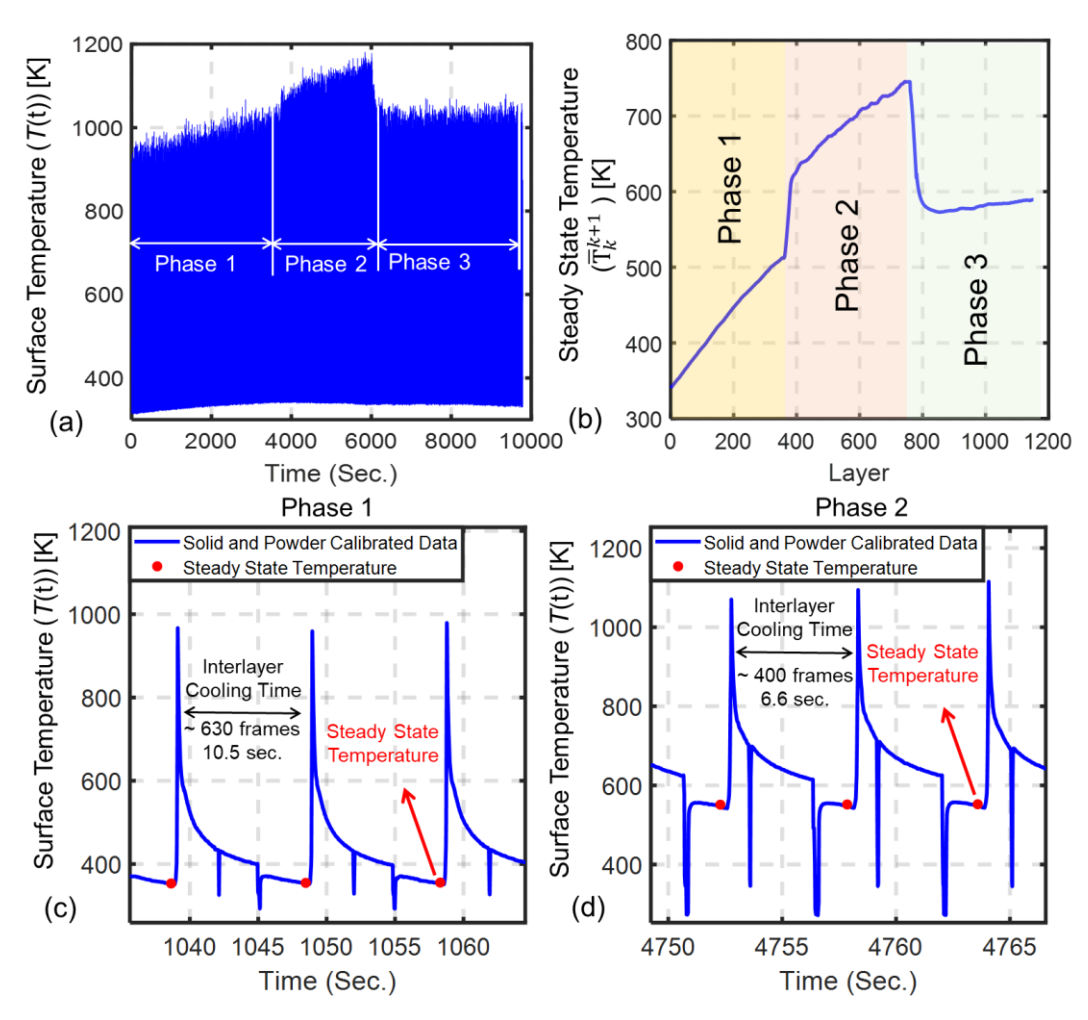


Figure 10: Data obtained from Build 1. (a) the surface temperature readings recorded by the long wave infrared (LWIR) camera, (b) smoothened trends obtained after considering the steady state temperature in the interlayer cooling time (ILCT). (c) and (d) the ILCT decreases from 10.5 seconds in Phase 1 to 6.6 seconds in Phase 2 leading to a large increase in the steady state temperature seen in (b).

4.1.2 Comparing the graph theory temperature predictions with experimental observations.

In Figure 11(a) maps the effect of changing the super layer thickness (SLT) on the steady state surface temperature distribution predicted by the graph theory approach for number of nodes N= 3000. In Figure 11(b), the converse case, i.e., the SLT is maintained constant (0.3 mm, 6 individual layers of 50 µm each) and the steady state surface temperature distribution with varying N is predicted. A more detailed sensitivity analysis determining the effect of N and SLT on the MAPE, RMSE, and computation time is reported in-depth in Appendix 1.

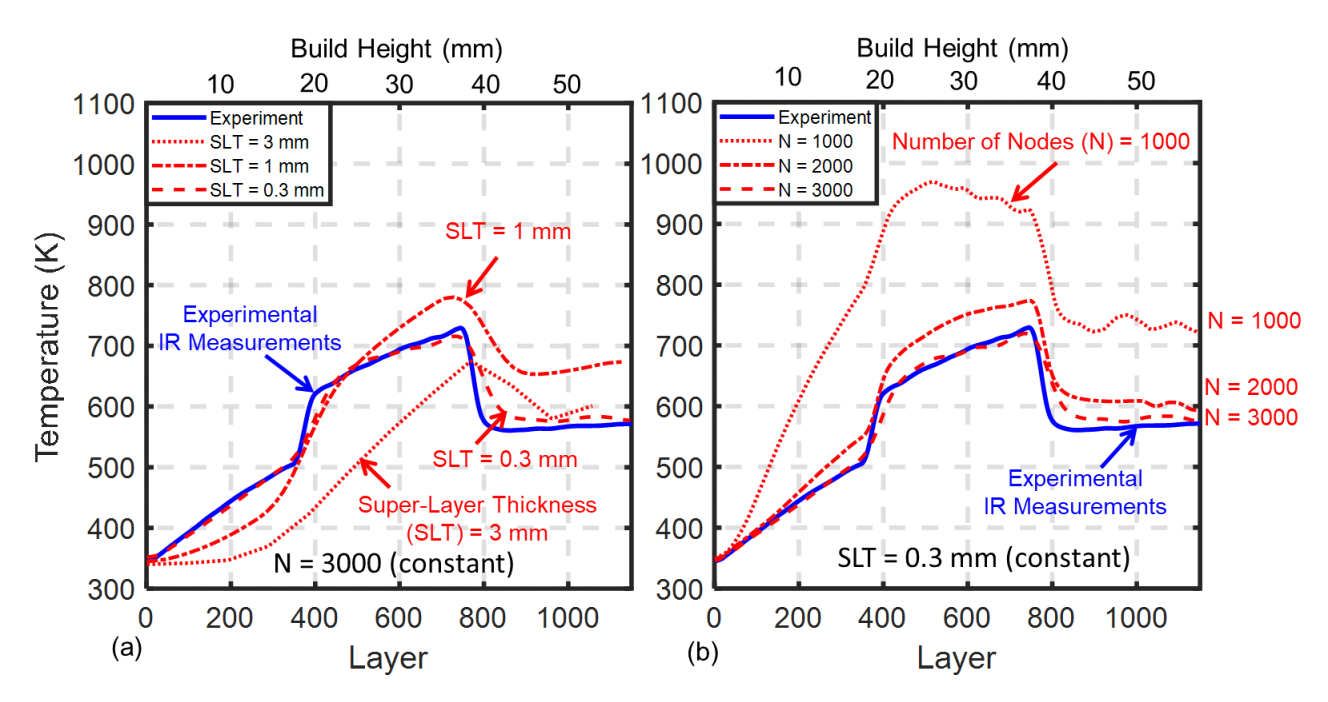


Figure 11: Representative steady state temperature trend predictions for Build 1 (cylinder). (a) The effect of the super layer thickness on the temperature trends predicted using graph theory with number of nodes fixed at N = 3000. (b) The effect of varying the number of nodes N at a fixed super layer thickness of 0.3 mm (consisting of 6 actual layers of 50 μ m each).

In general, the prediction accuracy improves (MAPE and RMSE reduces) as the SLT is decreased, and N is increased. However, the relationship is not linear. An amicable balance in both accuracy and computation time is obtained by setting SLT = 0.3 mm (6 individual layers) and N = 3000. The error under these conditions (MAPE) is close to 13%, and the results are obtained in approximately 26 minutes ($\approx 1/6^{th}$ of the actual build time of 171 minutes). The MAPE reduces to \sim 9% for N = 4000 and SLT = 0.3, however, the computational time increases to 65 minutes.

4.1.3 Comparison of graph theory temperature predictions with finite element analysis

The predictions from the graph theory approach are compared with finite element (FE) analysis in Figure 12 and Table 3. As explained in Sec. 3.6, to ensure equitable comparison, we implemented the super layer approach in a FE in a commercially software (Abaqus), the detailed implementation of the FE analysis is described in Ref. [9].

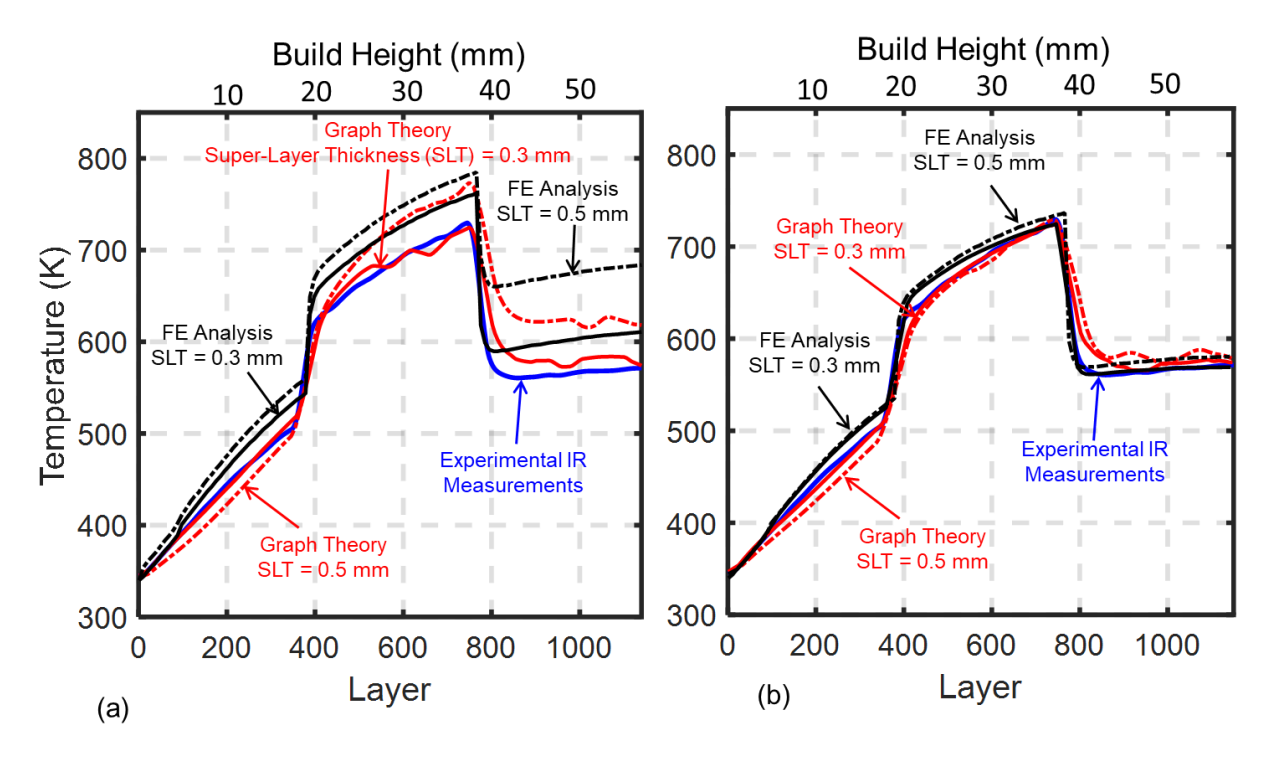


Figure 12. The FE and graph theory results compared for different super layer thicknesses (SLT) for Build 1. (a) FE and graph theory analysis with 3000 nodes, (b) FE and graph theory analysis with 5000 nodes.

In Figure 12(a), representative thermal trends for two super layer settings 0.3 mm (6 individual layers) and 0.5 mm (8 individual layers), with N=3000 for the graph theoretic approach are compared with FE analysis under identical conditions relative to the experimental temperature measurements. Likewise, Figure 12(b) shows the analysis repeated for N=5000. The comparison between FE and graph theory results is quantified in Table 3.

Table 3: Comparison of finite element (FE) and graph theory approaches with experimental data for Build 1 (cylinder). The actual build time is 171 minutes (10,260 seconds)

	Finite		Graph		Graph Theory		Finite		Graph Theory	
	Eler	nent	Theory				Element			
Nodes (N)	30	00	300	00	4000			5000		
Super Layer Thickness (SLT) [mm]	0.3	0.5	0.3	0.5	0.3	0.5	0.3	0.5	0.3	0.5
Computation Time [s]	2,048	1,347	1,655	949	3,912	2,209	10,446	6,053	7,270	4,176
MAPE (%)	16.7	29.4	13.8	18.2	8.7	11.5	9.1	9.4	8.6	10.4
RMSE (Kelvin, [K])	36.8	90.1	16.2	54.1	15.7	16.8	17.2	18.4	15.2	25.1

With N =3000, and super layer thickness (SLT) 0.3 mm, the MAPE for the FE analysis is approximately 16%, and the results are obtained within 2,048 seconds (34 minutes). Using the graph theory approach, the MAPE is 14%, and the trends are obtained in 1,655 seconds (27 minutes) of computation.

Next, we fix the MAPE of $\sim 9\%$, and RMSE 16.5 ± 1 K and compare the computational time for graph theory and FE approach for an identical resolution (SLT = 0.3). For the graph theory approach the MAPE and RMSE reduced to less than 9% and 16 K on increasing N = 4000 with corresponding computation time of 65 minutes. To achieve the same level of prediction error it requires the FE approach 5000 nodes, and nearly 175 minutes. Effectively, the graph theory approach requires 40% of the computation time of FE to reach approximately similar level of MAPE and RMSE with an identical level of resolution (super layer thickness). The computational advantage of the graph theory approach is retained when the number of nodes N = 5000 for both FE and graph theory; the graph theory approach converges $\sim 30\%$ faster than FE.

The graph theory approach is currently implemented in Matlab (an interpreted computer language) which does not allow multi-core processing, and the code is not optimized for parallelization. In contrast, the FE analysis is conducted in a commercial package (Abaqus). Porting the graph theory approach to a compiled language, such as C++ with code optimization will further increase its computational efficiency.

4.2 Results for Build 2

4.2.1 Thermal signatures acquired from the thermal camera.

The procedure described earlier in Sec. 3.4 is used to pre-process the thermal signatures obtained for Build 2. As shown in Figure 13(a), in Build 2, a gradual increase in the steady state surface temperature is observed. The ILCT increases with the build height (Figure 13(b)), because, as the top surface area increases, the time required to scan successive layers also increases.

Consequently, while the temperature increases for layers near the top, there is also more time for the layer to cool because it takes longer time for the laser to scan a larger surface area. Hence, there is a gradual increasing trend in surface temperature as the accumulation of heat near the top surface occurs concurrently with an increase in ILCT. The steady state surface temperature nearly reaches the liquidous temperature of 316L stainless steel (1600 K) The practical implication of Build 2 is that the process parameters must be adapted layer-by-layer as opposed to a fixed parameter set so that the part temperature remains consistent. This can be achieved by varying the scan pattern, laser power, and ILCT (by pausing the process between layers for a longer time).

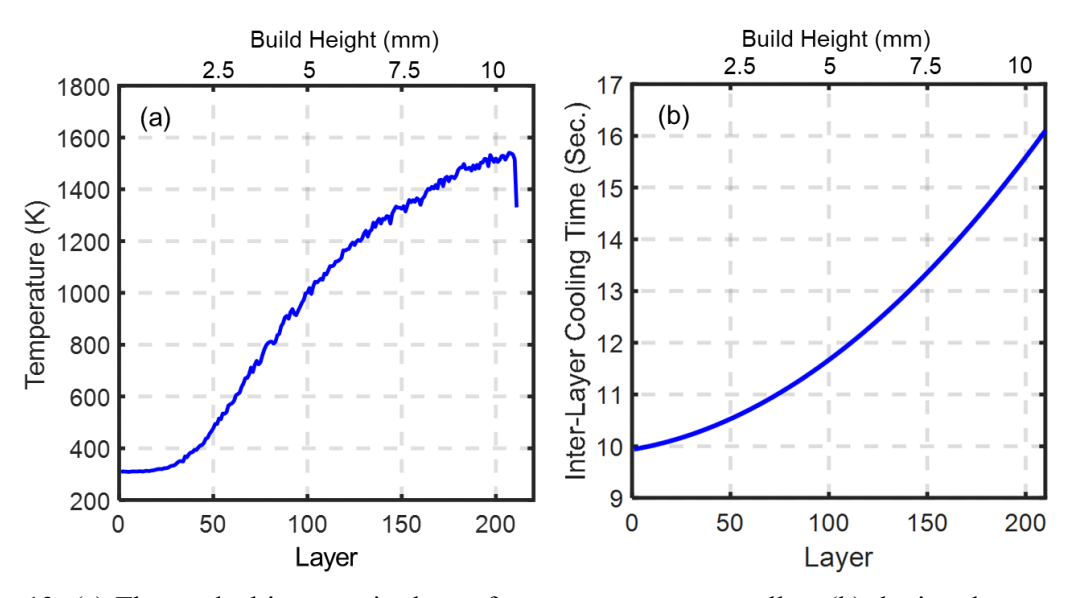


Figure 13: (a) The gradual increase in the surface temperature, as well as (b) the interlayer cooling time with the build height.

4.2.2 Comparison of graph theory temperature predictions with experimental observations.

The inverted cone shape is more complex than the cylinder as its cross-section area changes with the build height, and hence more number of nodes are required to capture the heat flux. As before, a smaller super layer thickness (SLT) and larger number of nodes both improve the accuracy of the solution.

Sensitivity analysis tracking the effect of number of nodes (N) and super layer thickness on MAPE, RMSE, and computation time is reported in Appendix 2. Representative results are shown in Figure 14. For instance, in Figure 14(a) when the number of nodes (N) is set at 4000, and the SLT is 0.2 mm the MAPE \sim 6%, and computation time is close to 41 minutes. In Figure 14(b) the SLT is held equal to 0.3 mm and N = 4000, which results in MAPE \sim 7%, and computation time \sim 33 minutes; the actual build time for Build 2 is close to 51 minutes.

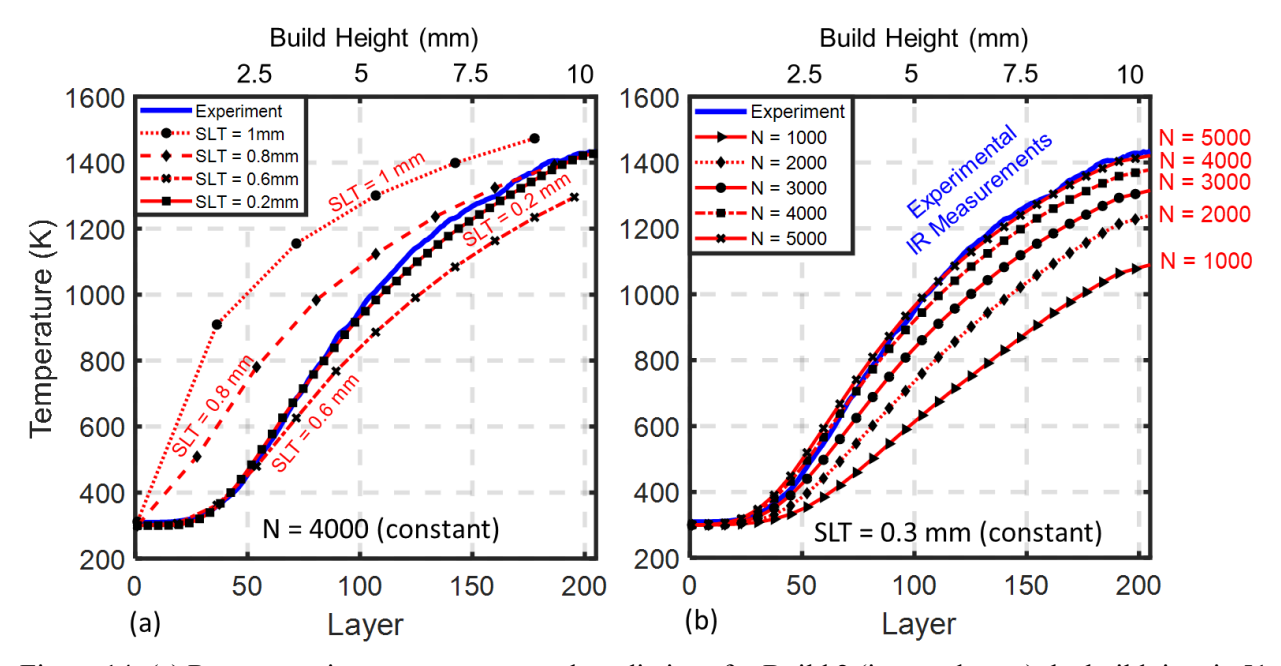


Figure 14: (a) Representative temperature trend predictions for Build 2 (inverted cone) the build time is 51 minutes. The effect of the super layer thickness on the temperature trends predicted using graph theory with number of nodes fixed at N = 4000. (b) The effect of varying the number of nodes N at a fixed super layer thickness of 0.3 mm (6 actual layers of 50 μ m each).

4.2.3 Comparison of graph theory temperature predictions with finite element analysis

The graph theory-derived predictions for Build 2 are compared with the FE analysis in Figure 15 and Table 4. For equitable comparison, the FE analysis is set to a super layer thickness of 0.2 mm and 0.3 mm, and the number of nodes (N) is set at 4000. As apparent from Figure 15(a), both the FE and graph theory approaches track the increasing surface temperature trends evident in the experimental data. Furthermore, for the results shown in Figure 15(b) we increased number of nodes (N) for the FE analysis until it converged to a nearly identical accuracy level of accuracy in terms of MAPE and RMSE observed for graph theory.

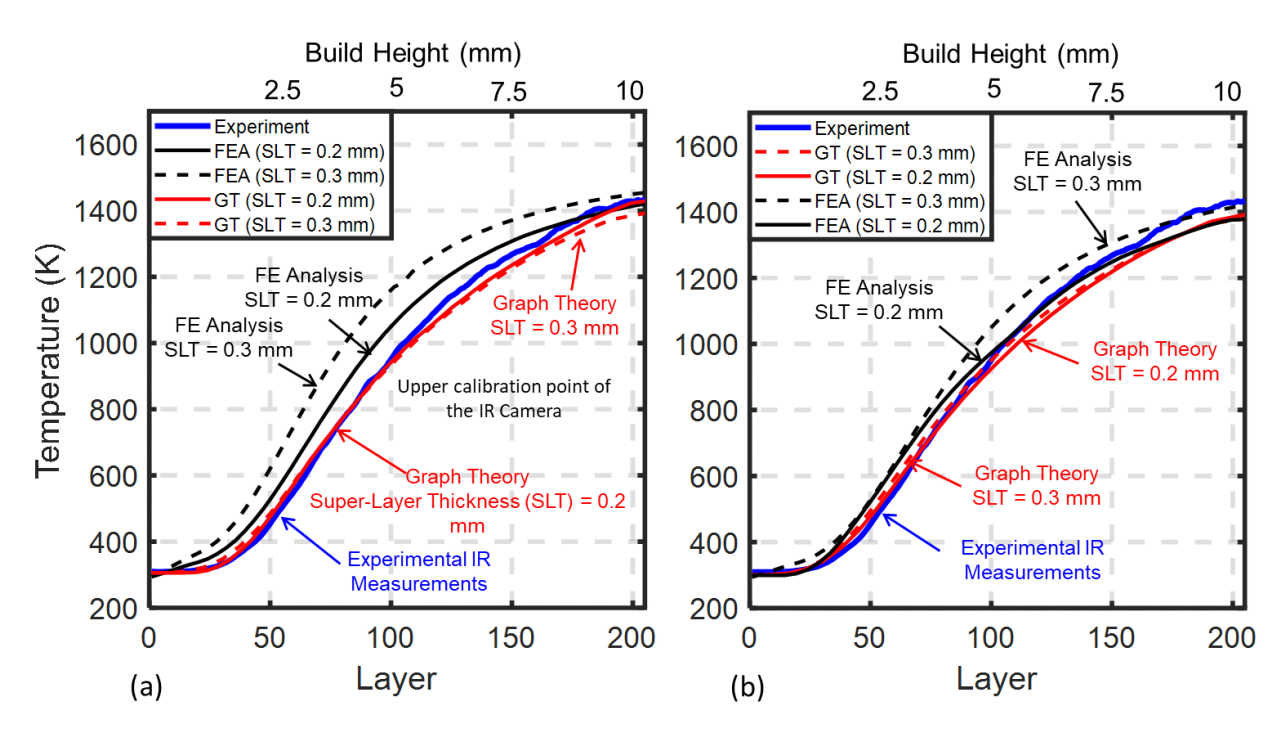


Figure 15: The temperature trends predicted using the FE and graph theory approach compared for different super layer thicknesses (SLT) and number of nodes (N) for Build 2. Abaqus is used for simulating the deposition of super layers in the FE analysis. (a) N=4000 for both the graph theory and FE approaches. (b) N=6800 for FE, and N=5000 for graph theory.

As exemplified in Figure 15, and quantitatively in Table 4, for a fixed resolution (SLT), and for an RMSE of 28.5 ± 1 K, and MAPE $\sim 6\%$, the FE analysis required N = 6800 and 96 minutes of computation time. By contrast, for the foregoing degree of prediction error, the graph theory

approach required N = 4000, and converged in 41 minutes. In other words, the graph theory required 40% fewer nodes and converged within 40% of the time required by FE. These results affirm the computational advantages of the graph theory approach over FE.

Table 4: Comparison of finite element and graph theoretic approaches for Build 2 (inverted cone).

	Finite		Graph Theory		Graph		Finite	
	Element				Theory		Element	
Number of nodes (N)	4000		4000		5000		6800	
Super Layer Thickness (mm)	0.2	0.3	0.2	0.3	0.2	0.3	0.2	0.3
Computation Time [s]	3,274	2,948	2,471	2,081	4,784	4,045	5,982	5,034
MAPE (%)	9.6	15.9	5.73	6.8	3.72	4.54	6.2	10.9
RMSE [K]	42.1	76.4	26	32.8	12.15	20.7	27.6	43.8

4.3 Comparison of graph theory predictions with FE analysis for point in the interior of the part

We compare the graph theory and FE predictions for a point in the interior volume of the two builds. The results, shown in Figure 16, substantiate that both the graph theory and FE approaches capture the cyclical heating and cooling characteristic of LPBF as material is deposited and melted layer-upon-layer.

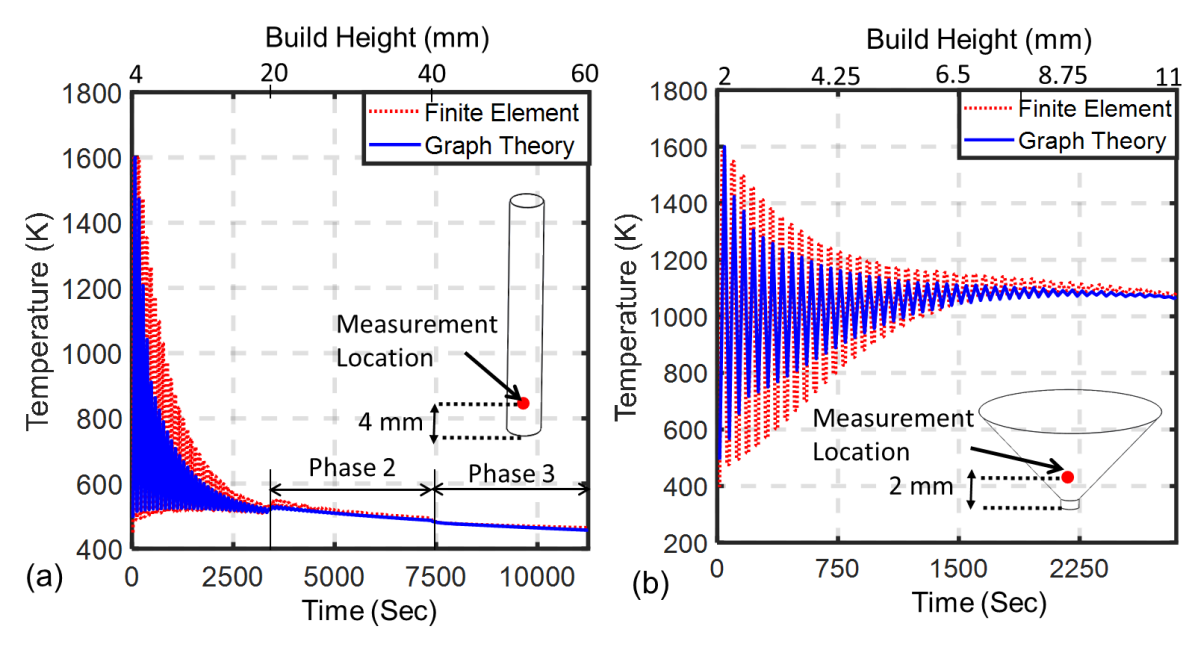


Figure 16: Comparison of the FE and graph theory predictions in the interior of the build volume (a) Build 1, the measurement point is on the axis, 4 mm from the bottom. The number of nodes N=3000 and

superlayer thickness (SLT) is 0.3 mm (b) Build 2, the measurement point is on the axis, 2 mm from the bottom; N = 4000 and SLT is 0.2 mm.

In the case of Build 1, Figure 16(a), the measurement (sample) location for testing both FE and graph theory models is on the central axis cylinder, 4 mm from the bottom (viz., 1/5th of the height of Phase 1 build of 20 mm; the total build height over the three layers is 60 mm). In Build 2, we observe the temperature at a location on the central axis of the cone, and at a distance of 2 mm from the bottom (~1/5th of the build height of 11 mm). The x-axis of Figure 16 corresponds to the build height, in the context of time. Closer examination of the plots, particularly Figure 16(b), shows a close alignment in the peaks and valleys of the temperature predictions from the graph theory approach and FE predictions.

Close examination of Figure 16(a), in the context of Build 1, reveals that there is a slight increase in the temperature corresponding to start of Phase 2, and decrease at the start of Phase 3. The change in temperature at the interior point shown in Figure 16(a), corresponding to the phases of Build 1 is not as prominent as in the steady state surface temperature plots in Figure 10 due to attenuation of the temperature signature as the part grows in size. The attenuation of the thermal signature harkens to the limitations in acquiring the temperature data by embedding a thermocouple inside of the substrate discussed in Sec. 2.1.

Concerning Build 2, in Figure 16(b) the attenuation again affects the cyclical pattern as the build progresses. However, the temperature at the measurement point for Build 2 does not decrease as in Build 1, because, as explained in the context of Figure 13, Sec. 0, the surface temperature for the conical test part increases continually throughout the process.

5 Conclusions

This work provides experimental evidence to substantiate the computational efficiency and accuracy of the graph theoretic approach proposed in our previous work [5]. We arrive at the following conclusions through two experimental builds conducted in the specific context of the laser powder bed fusion (LPBF) AM process.

- (1) In Build 1, a cylindrical part 8 mm diameter, 60 mm vertical build height is processed with a phased build plan, such that other parts are intermittently added and removed during the build. Consequently, the interlayer cooling time varies over the 1200 layers of the build, which in turn influences the thermal history and microstructure.
 - The graph theoretic approach predicts the resulting complex thermal history within 65 minutes with a mean absolute percentage error (MAPE) less than 10% and 16 K root mean squared error (RMSE), which is substantially the actual build time of 171 minutes. For a comparable level of MAPE and RMSE a coarse finite element approximation requires 177 minutes.
 - From a practical perspective, Build 1 shows that the graph theory approach is capable of emulating a complex multi-part build plan with test parts being removed and added during the process.
- (2) In Build 2, a conical part of diameter 20 mm and vertical build height 11 mm is processed in a way such that the diameter of its circular end progressively increases with the build height (an inverted cone). The actual build time is 51 minutes. The steady state surface temperature for this test part gradually increases with the addition of new layers, despite processing under constant LPBF parameters. The graph theory approach predicts this increasing steady state temperature trends within 41 minutes the surface temperature distribution with MAPE less

than 7% and RMSE of 32 K relative to the experimental observations. In contrast, for nearly identical level of MAPE and RMSE, the finite element approach requires 96 minutes.

The graph theory approach has the potential to facilitate physics-based optimization of process parameters (laser power, hatch pattern, etc.), build strategy, support placement, etc., to minimize warping and distortion. In our forthcoming works we will validate the graph theory approach for complex geometry parts. However, the prediction of microstructural evolution with graph theory remains a challenging problem. This is because the microstructure evolution is a function of both the part-level temperature and the meltpool-level thermal-fluid flow phenomena. The graph theory approach currently does not incorporate meltpool-level phenomena.

Acknowledgments

One of the authors (PKR) thanks the NSF for funding his research through the following grants CMMI-1719388, CMMI-1739696, CMMI-1752069, and OIA-1929172 at University of Nebraska-Lincoln. Specifically, the concept of using graph theory for modeling in metal additive manufacturing applications is funded through CMMI-1752069.

References Cited

- [1] François, M. M., Sun, A., King, W. E., Henson, N. J., Tourret, D., Bronkhorst, C. A., Carlson, N. N., Newman, C. K., Haut, T., Bakosi, J., Gibbs, J. W., Livescu, V., Vander Wiel, S. A., Clarke, A. J., Schraad, M. W., Blacker, T., Lim, H., Rodgers, T., Owen, S., Abdeljawad, F., Madison, J., Anderson, A. T., Fattebert, J. L., Ferencz, R. M., Hodge, N. E., Khairallah, S. A., and Walton, O., 2017, "Modeling of additive manufacturing processes for metals: Challenges and opportunities," Opinion Current in Solid State and Materials Science. 21(4), pp. 198-206.doi:https://doi.org/10.1016/j.cossms.2016.12.001
- [2] DebRoy, T., Wei, H. L., Zuback, J. S., Mukherjee, T., Elmer, J. W., Milewski, J. O., Beese, A. M., Wilson-Heid, A., De, A., and Zhang, W., 2018, "Additive manufacturing of metallic components Process, structure and properties," Progress in Materials Science, 92, pp. 112-224.doi:https://doi.org/10.1016/j.pmatsci.2017.10.001
- [3] Foteinopoulos, P., Papacharalampopoulos, A., and Stavropoulos, P., 2018, "On thermal modeling of Additive Manufacturing processes," CIRP Journal of Manufacturing Science and Technology, 20, pp. 66-83.doi:https://doi.org/10.1016/j.cirpj.2017.09.007

- [4] Sames, W. J., List, F., Pannala, S., Dehoff, R. R., and Babu, S. S., 2016, "The metallurgy and processing science of metal additive manufacturing," International Materials Reviews, 61(5), pp. 315-360
- [5] Yavari, M. R., Cole, K., and Rao, P., 2019, "Thermal Modeling in Metal Additive Manufacturing using Graph Theory," ASME Transactions, Journal of Manufacturing Science and Engineering, 141(7), pp. 071007-071027.doi:10.1115/1.4043648
- [6] Goldak, J., Chakravarti, A., and Bibby, M., 1984, "A new finite element model for welding heat sources," Metallurgical Transactions B, 15(2), pp. 299-305.doi:10.1007/bf02667333
- [7] Goldak, J. A., and Akhlaghi, M., 2005, "Computer simulation of welding processes," Computational Welding Mechanics, pp. 16-69
- [8] Williams, R. J., Piglione, A., Rønneberg, T., Jones, C., Pham, M.-S., Davies, C. M., and Hooper, P. A., 2019, "In-situ thermography for laser powder bed fusion: effects of layer temperature on porosity, microstructure and mechanical properties.," Additive Manufacturing, (Accepted, Under 2nd Review)
- [9] Williams, R. J., Davies, C. M., and Hooper, P. A., 2018, "A pragmatic part scale model for residual stress and distortion prediction in powder bed fusion," Additive Manufacturing, 22, pp. 416-425.doi:https://doi.org/10.1016/j.addma.2018.05.038
- [10] Yan, Z., Liu, W., Tang, Z., Liu, X., Zhang, N., Li, M., and Zhang, H., 2018, "Review on thermal analysis in laser-based additive manufacturing," Optics & Laser Technology, 106, pp. 427-441.doi:https://doi.org/10.1016/j.optlastec.2018.04.034
- [11] Tapia, G., and Elwany, A., 2014, "A Review on Process Monitoring and Control in Metal-Based Additive Manufacturing," Journal of Manufacturing Science and Engineering, 136(6), pp. 060801-060801-060810.doi:10.1115/1.4028540
- [12] Dunbar, A. J., Denlinger, E. R., Gouge, M. F., Simpson, T. W., and Michaleris, P., 2017, "Comparisons of laser powder bed fusion additive manufacturing builds through experimental in situ distortion and temperature measurements," Additive Manufacturing, 15, pp. 57-65.doi:https://doi.org/10.1016/j.addma.2017.03.003
- [13] Dunbar, A., Denlinger, E., Heigel, J., Michaleris, P., Guerrier, P., Martukanitz, R., and Simpson, T., 2016, "Development of experimental method for in situ distortion and temperature measurements during the laser powder bed fusion additive manufacturing process," Additive Manufacturing, 12, pp. 25-30
- [14] Promoppatum, P., Yao, S.-C., Pistorius, P. C., Rollett, A. D., Coutts, P. J., Lia, F., and Martukanitz, R., 2018, "Numerical modeling and experimental validation of thermal history and microstructure for additive manufacturing of an Inconel 718 product," Progress in Additive Manufacturing, 3(1), pp. 15-32.doi:10.1007/s40964-018-0039-1
- [15] Wood, N., Mendoza, H., Boulware, P., and Hoelzle, D. J., 2019, "Interrogation of mid-build internal temperature distributions within parts being manufactured via the powder bed fusion process," 30th Solid Freeform Fabrication Conference, Austin, TX, pp. 1445-1481
- [16] Heigel, J. C., Michaleris, P., and Reutzel, E. W., 2015, "Thermo-mechanical model development and validation of directed energy deposition additive manufacturing of Ti–6Al–4V," Additive Manufacturing, 5, pp. 9-19.doi:https://doi.org/10.1016/j.addma.2014.10.003

- [17] Yavari, R., Severson, J., Gaikwad, A., Cole, K., and Rao, P., 2019, "Predicting Part-Level Thermal History in Metal Additive Manufacturing Using Graph Theory: Experimental Validation With Directed Energy Deposition of Titanium Alloy Parts," ASME 2019 14th International Manufacturing Science and Engineering Conference, doi:10.1115/msec2019-3034.
- [18] Lane, B., Moylan, S., Whitenton, E. P., and Ma, L., 2016, "Thermographic measurements of the commercial laser powder bed fusion process at NIST," Rapid Prototyping Journal, 22(5), pp. 778-787.doi:doi:10.1108/RPJ-11-2015-0161
- [19] Moylan, S., Whitenton, E., Lane, B., and Slotwinski, J., 2014, "Infrared thermography for laser-based powder bed fusion additive manufacturing processes," AIP Conference Proceedings, 1581(1), pp. 1191-1196.doi:10.1063/1.4864956
- [20] Everton, S. K., Hirsch, M., Stravroulakis, P., Leach, R. K., and Clare, A. T., 2016, "Review of in-situ process monitoring and in-situ metrology for metal additive manufacturing," Materials & Design, 95, pp. 431-445.doi:https://doi.org/10.1016/j.matdes.2016.01.099
- [21] Krauss, H., Zeugner, T., and Zaeh, M. F., 2015, "Thermographic process monitoring in powderbed based additive manufacturing," AIP Conference Proceedings, 1650(1), pp. 177-183.doi:10.1063/1.4914608
- [22] Mani, M., Lane, B. M., Donmez, M. A., Feng, S. C., and Moylan, S. P., 2017, "A review on measurement science needs for real-time control of additive manufacturing metal powder bed fusion processes," International Journal of Production Research, 55(5), pp. 1400-1418.doi:10.1080/00207543.2016.1223378
- [23] Usamentiaga, R., Venegas, P., Guerediaga, J., Vega, L., Molleda, J., and Bulnes, F. G., 2014, "Infrared Thermography for Temperature Measurement and Non-Destructive Testing," Sensors, 14(7), pp. 12305-12348
- [24] Murphy, R. D., and Forrest, E. C., 2016, "A Review of In-situ Temperature Measurements for Additive Manufacturing Technologies," Sandia National Lab.(SNL-NM), Albuquerque, NM (United States).
- [25] Rodriguez, E., Mireles, J., Terrazas, C. A., Espalin, D., Perez, M. A., and Wicker, R. B., 2015, "Approximation of absolute surface temperature measurements of powder bed fusion additive manufacturing technology using in situ infrared thermography," Additive Manufacturing, 5, pp. 31-39.doi:https://doi.org/10.1016/j.addma.2014.12.001
- [26] Yavari, M. R., Cole, K. D., and Rao, P. K., 2019, "Design Rules for Additive Manufacturing Understanding the Fundamental Thermal Phenomena to Reduce Scrap," Procedia Manufacturing, 33, pp. 375-382.doi:https://doi.org/10.1016/j.promfg.2019.04.046

Appendix 1
Build 1 – Cylinder built in multiple phases.

60~mm build height, 1,200 layers, $50~\mu\text{m}$ layer thickness, 171 minutes (10,260 sec) build time

Number of Nodes	Super-Layer Thickness	Number of Super- layers	RMSE (K) (Std. Dev. Over three repetitions)	MAPE (Std. Dev. Over three repetitions)	Mean Computation Time in seconds. (Std. Dev over three repetitions)
	3	20	68.57 (8.3)	30.48 (2.2)	289 (2.6)
	2	30	46.78 (7.9)	22.45 (2.4)	699 (7.3)
	1	60	37.22 (6.3)	17.24 (1.3)	1323 (11.4)
5000	0.8	75	37.47 (7.2)	14.85 (1.5)	2086 (15.7)
3000	0.6	100	33.08 (7.0)	14.52 (1.2)	3037 (18.3)
	0.5	120	25.18 (6.3)	10.42 (1.1)	4176 (20.4)
	0.4	150	20.75 (3.7)	9.48 (0.8)	5500 (24.2)
	0.3	200	15.27 (1.3)	8.67 (0.4)	7270 (29.5)
	3	20	79.06 (13.6)	29.46 (3.2)	169 (1.4)
	2	30	69.15 (12.3)	21.44 (3.0)	384 (2.2)
	1	60	44.07 (9.5)	18.21 (2.1)	727 (5.4)
4000	0.8	75	42.55 (8.5)	16.46 (1.6)	1125 (10)
4000	0.6	100	35.41 (8.4)	15.88 (1.4)	1636 (14.2)
	0.5	120	16.87 (8.5)	11.54 (1.4)	2209 (16.8)
	0.4	150	15.29 (7.9)	9.67(1.2)	2971 (17.2)
	0.3	200	15.73 (2.4)	8.75 (0.8)	3912 (23)
	3	20	74.44 (14.5)	27.64 (3.4)	75 (0.4)
	2	30	64.38 (13.7)	22.54 (2.8)	166 (1.2)
	1	60	63.76 (13.6)	21.48 (2.8)	311 (2.4)
3000	0.8	75	57.94 (12.9)	20.55 (2.5)	481 (3.2)
3000	0.6	100	56.93 (7.3)	20.24 (1.5)	696 (6.3)
	0.5	120	54.1 (7.9)	18.2 (1.9)	949 (7.8)
	0.4	150	26.18 (5.5)	15.89 (1.3)	1254 (9.4)
	0.3	200	16.28 (2.3)	13.81 (0.9)	1655 (13.8)
	3	20	77.52 (16.0)	31.82 (4.7)	27 (0.2)
	2	30	52.69 (15.4)	30.75 (4.2)	56 (0.3)
	1	60	51.28 (12.1)	25.17 (3.1)	98 (0.7)
2000	0.8	75	49.38 (12.5)	23.22 (3.6)	152 (1)
2000	0.6	100	48.34 (12.2)	20.85 (3.2)	217 (1.4)
	0.5	120	41.68 (10.8)	18.72 (2.7)	298 (1.7)
	0.4	150	38.64 (10.5)	17.37 (2.5)	383 (1.9)
	0.3	200	30.96 (11.2)	16.38 (3.1)	501 (2.7)
	3	20	88.64 (19.4)	35.24 (5.9)	9 (0.1)
	2	30	54.16 (18.8)	35.63 (6.5)	14 (0.1)
	1	60	54.58 (16.3)	30.58 (4.2)	22 (0.2)
1000	0.8	75	52.54 (14.7)	24.35 (3.5)	31 (0.2)
	0.6	100	45.06 (13.5)	21.52 (3.3)	42 (0.3)
	0.5	120	37.52 (16.7)	20.38 (4.5)	53 (0.4)
	0.4	150	37.10 (17.4)	19.09 (5.2)	71 (0.5)
	0.3	200	34.24 (14.6)	19.38 (4.8)	92 (0.7)

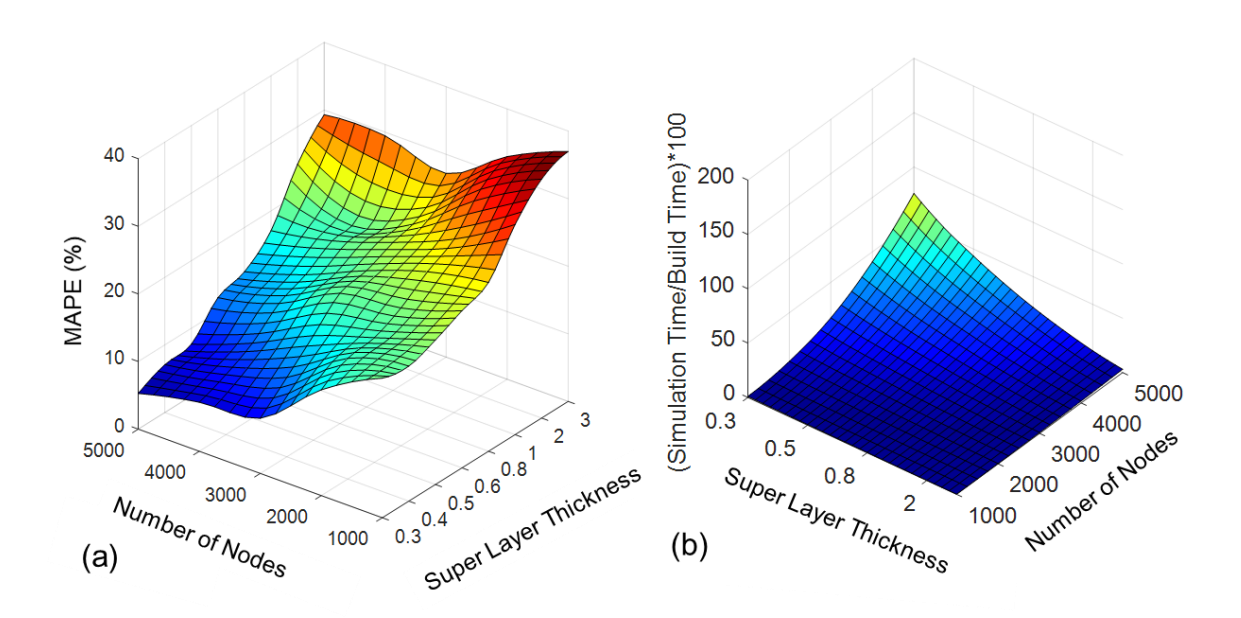


Figure 17: Sensitivity analysis for Build 1. (a)The effect of the super layer thickness (SLT) in mm and number of nodes (N) used in the graph theory approach on the error vis-à-vis experimental data. (b) The ratio of the simulation time to build time as a percentage, versus N and SLT. The decrease in super layer thickness and increase in number of nodes improves the prediction accuracy, but at the cost of computation time.

Appendix 2
Build 2 – Inverted Cone.

11 mm build height, 220 layers, 50 µm layer thickness, 51 minutes (3060 sec) build time

1 1 111111					(3060 sec) build time
Number of	Super-	Number	RMSE (K)	MAPE (Std. Dev.	Mean Computation Time
Nodes	Layer	of Super-	(Std. Dev. Over	Over three	in seconds (Std. Dev over
	Thickness	layers	three repetitions)	repetitions)	three repetitions).
	1	11	267.07 (30.6)	38.54 (4.5)	434 (2.4)
	0.9	12	231.71 (27.4)	37.45 (4.2)	913 (6.4)
	0.8	14	134.86 (15.2)	27.21 (3.4)	1420 (10.3)
	0.7	15	94.52 (10.4)	24.64 (2.5)	1981 (15.5)
5000	0.6	18	64.94 (8.4)	11.77 (1.7)	2374 (18)
	0.5	22	39.18 (4.2)	10.87 (1.5)	2865 (19.1)
	0.4	28	26.54 (4.4)	9.21 (1.5)	3436 (21.7)
	0.3	36	20.71 (2.2)	4.54 (0.6)	4045 (25.7)
	0.2	55	12.15 (1.4)	3.72 (0.7)	4784 (26.3)
	1	11	302.97 (35.2)	49.43 (5.2)	237 (1.6)
	0.9	12	231.03 (26.4)	41.09 (4.6)	470 (3.5)
	0.8	14	175.75 (19.2)	35.93 (3.4)	720 (5.3)
	0.7	15	101.07 (11.8)	25.84 (2.4)	1003 (7.7)
4000	0.6	18	93.28(12.0)	20.97 (2.6)	1198 (8.2)
	0.5	22	75.47 (7.8)	15.46 (1.4)	1442 (9.9)
	0.4	28	50.49 (7.2)	11.03 (1.2)	1752(12.2)
	0.3	36	35.43 (2.4)	6.84 (0.5)	2081 (14.2)
	0.2	55	26.00 (2.8)	5.73 (0.6)	2471 (15)
	1	11	357.36 (38.5)	41.76 (4.9)	136 (1)
	0.9	12	351.88 (37.1)	40.64 (4.6)	258 (1.5)
	0.8	14	226.31 (23.4)	35.24 (3.6)	387 (2.8)
	0.7	15	127.97 (14.4)	28.21 (2.4)	521 (3.1)
3000	0.6	18	154.19 (16.2)	24.19 (2.7)	615 (4.2)
	0.5	22	128.79 (13.8)	20.64 (2.5)	729 (4.8)
	0.4	28	108.46 (12.0)	18.72 (1.6)	870 (5.5)
	0.3	36	101.20 (11.4)	17.13 (1.5)	1017 (6.8)
	0.2	55	94.56 (11.5)	12.21 (2.1)	1192 (7.3)
	1	11	343.17 (41.2)	51.46 (6.3)	41 (0.3)
	0.9	12	265.67 (29.7)	34.51 (4.2)	79 (0.5)
	0.8	14	201.36 (23.2)	34.88 (3.5)	119 (0.8)
	0.7	15	148.04 (18.6)	31.54 (3.1)	162 (0.9)
2000	0.6	18	154.16 (17.3)	30.46 (4.3)	193 (1.1)
	0.5	22	128.77 (11.3)	28.40 (3.5)	231 (1.5)
	0.4	28	125.54 (10.3)	26.84 (2.5)	278 (1.6)
	0.3	36	120.45 (9.5)	24.48 (2.7)	325 (2.4)
	0.2	55	98.48 (9.2)	21.37 (2.1)	381 (2.7)
	1	11	348.57 (48.1)	57.41 (7.3)	35 (0.2)
1000	0.9	12	327.99 (41.9)	51.20 (5.7)	45 (0.3)
	0.8	14	261.20 (32.3)	50.49 (5.4)	55 (0.4)
	0.7	15	253.21 (19.8)	48.34 (4.2)	65 (0.5)
	0.6	18	246.07 (23.4)	43.24 (4.5)	73 (0.6)
	0.6	22	203.12 (26.4)	35.11 (4.2)	82 (0.6)
	0.3	28	167.88 (18.4)	30.24 (4.2)	93 (0.7)
	0.4	36	165.79 (18.5)	27.71 (4.8)	` '
	0.3			` /	104 (0.8)
	U.Z	55	111.53 (17.4)	26.21 (4.2)	116 (0.8)

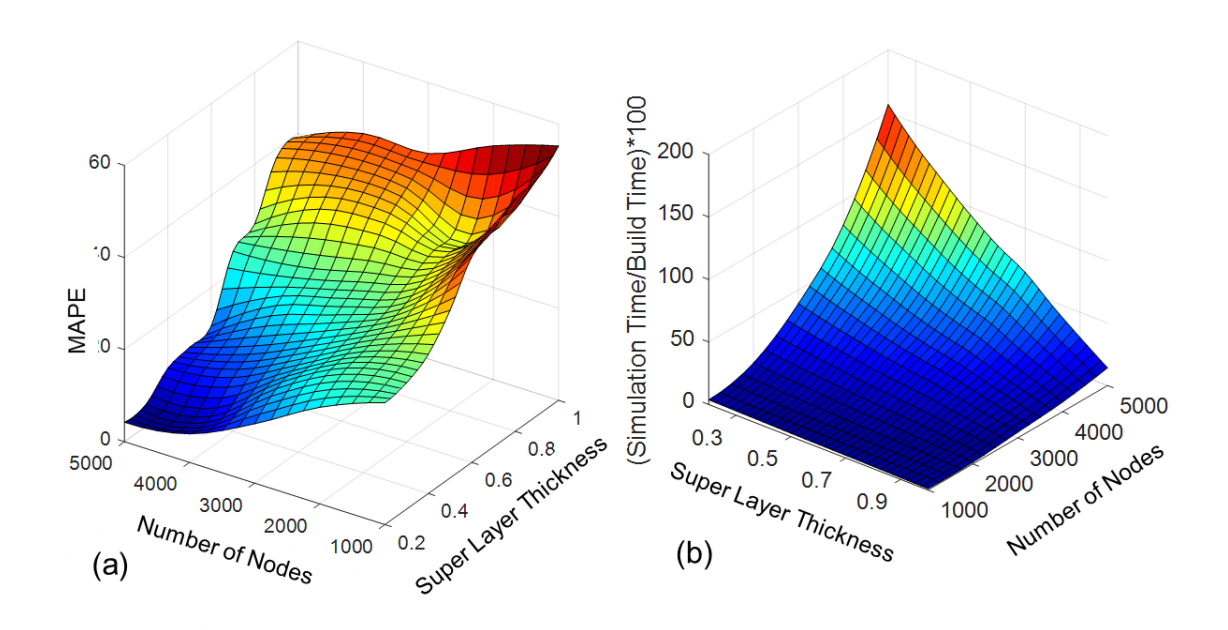


Figure 18: Sensitivity analysis for Build 2. (a) The effect of the super layer thickness (SLT) in mm and number of nodes (N) used in the graph theoretic approach on the error vis-à-vis experimental data. (b) The ratio of the simulation time to build time as a percentage, versus N and SLT. The decrease in super layer thickness and increase in number of nodes improves the prediction accuracy, but at the cost of computation time.